Preliminary Monte Carlo study of CZT response to BNCT (n+γ) background

S. Altieri[1][2], S. Fatemi[2], S. Bortolussi[1][2], C. Magni[1][2], I. Postuma[2] and N. Protti[2](*)

[1] *Dipartimento di Fisica, Università di Pavia - Pavia, Italy*
[2] *INFN, Sezione di Pavia - Pavia, Italy*

Summary. — Boron Neutron Capture Therapy (BNCT) effectiveness depends on the therapeutic dose delivered in tumour when targeted by a sufficient amount of ^{10}B atoms and exposed to a proper flux of thermal neutrons. Presently these quantities are measured indirectly. The availability of an *in vivo* and real time dose monitoring tool would be a tremendous achievement to fully exploit BNCT. To this end, a Single-Photon Emission Computed Tomography (SPECT) can measure the 478 keV γ-ray emitted after 94% of ^{10}B capture reactions. Presently, the Italian National Institute of Nuclear Physics (INFN) is supporting the $3CaTS$ project whose aim is to develop a dedicated BNCT-SPECT based on CdZnTe (CZT) semiconductor detectors. A BNCT-SPECT must operate in a highly intense (n + γ) radiation field. Thus, it is important to study the response of CZT detectors when working in such challenging conditions. In the present work we focused on three main aspects: i) the spectra of the radiation background expected in an accelerator-based BNCT treatment room; ii) the interaction of the thermal neutrons with cadmium present in the crystal; iii) the estimation of the recorded photon counts spectrum when a 478 keV photon source is simulated inside a tissue equivalent phantom.

1. – Introduction

Boron Neutron Capture Therapy (BNCT) is a binary cell-level localized hadrontherapy which is able to selectively destroy malignant cells while sparing the normal tissues. BNCT consists of the administration of a ^{10}B-enriched molecule to the patient and the subsequent irradiation of the tumour selectively targeted by the boronated drug with low-energy neutrons. The induced ^{10}B capture of thermal neutrons produces a couple of highly biologically effective particles (an α-particle and a ^{7}Li recoil nucleus), which

(*) Corresponding author. E-mail: nicoletta.protti@unipv.it

are high LET radiations (between 150 and $180\,\text{keV}/\mu\text{m}$) thus having small ranges in tissue (less than $10\,\mu\text{m}$), comparable to the mean cell diameter thus ensuring a cell-level selectivity [1].

BNCT effectiveness strongly depends on the therapeutic dose deposited locally by the $^{10}\text{B(n,}\alpha)^7\text{Li}$ reactions. The *in vivo* and real time measurement of this quantity during patient irradiation is a fundamental issue to optimise and fully exploit the BNCT advantages in cancer treatment.

Presently, therapeutic dose estimation in BNCT goes through the independent measurement of ^{10}B microscopic concentration on the one hand, and thermal neutron flux on the other hand. Both these quantities are known by indirect and off-line methods [2,3] which can partly justify the inhomogeneity of clinical outcomes even between patients treated inside the same trial. To significantly improve our capability of detecting and monitoring BNCT therapeutic dose, several teams are trying to exploit the $478\,\text{keV}$ disexcitation photon emitted by the 94% of ^7Li recoil nuclei thanks to a BNCT-dedicated Single-Photon Emission Computed Tomography (SPECT) [4-9].

Due to the specific characteristics of the single-photon emission after ^{10}B captures, the widely diffused Anger camera (also known as gamma camera) technology of conventional ^{99m}Tc SPECT is not directly exportable to BNCT. Besides, the counting rate of $478\,\text{keV}$ γ-rays in BNCT is expected to be pretty low, being necessarily constrained to the microscopic amount of ^{10}B inside cells (magnitude of *ppms*). In addition, the SPECT acquisition should be performed when the neutron source is turned on. This leads to a significant radiation background made of neutrons and photons of different origins. First of all, the unattenuated and scattered primary beam particles. Then, the secondary radiations produced by the incident beam in its interaction with the patient's body and treatment room walls. In particular, the former leads to: thermalization and scattering of the primary neutron component, scattering of primary beam photon contamination and finally to the in-tissue, local production of $2.2\,\text{MeV}$ γ-rays by the thermal capture reaction on the ^1H isotope together with the $478\,\text{keV}$ signal coming from the low ^{10}B accumulation in normal tissues. Concerning the effect of the room walls, they can impact on radiation background through several processes, *i.e.*, attenuation, scattering or emission of secondary photons due to neutron activation of their elemental composition.

For what stated, it is clear that to properly develop a BNCT-SPECT we must take into account the radiation $(n + \gamma)$ background unavoidably present in the patient treatment room of any BNCT facility and carefully understand how it influences the performance of the detector chosen for the SPECT imager.

2. – Materials and methods

Since 2017 the Italian National Institute of Nuclear Physics (INFN) has funded the $3CaTS$ project whose goal is to develop an innovative highly segmented prototype of a CdZnTe (CZT) solid-state photon detector to be used as spectrometer with 3D spatial resolution capability in the range from few tens of keV up to 1 MeV. The prototype should be compliant with the requirements defined by different applications fields, including: medical application for dedicated BNCT-SPECT; hard X- and soft γ-rays astronomy; fine spectroscopic experiments in fundamental physics.

We chose to base our work on the CZT technology thanks to its good energy resolutions in the energy range of interest, high detection efficiency even with small volume crystals (due to the effective high atomic number, $Z \approx 50$, and high density, $\rho = 5.78\,\text{g}\cdot\text{cm}^{-3}$), and the possibility of working without any cooling system because of
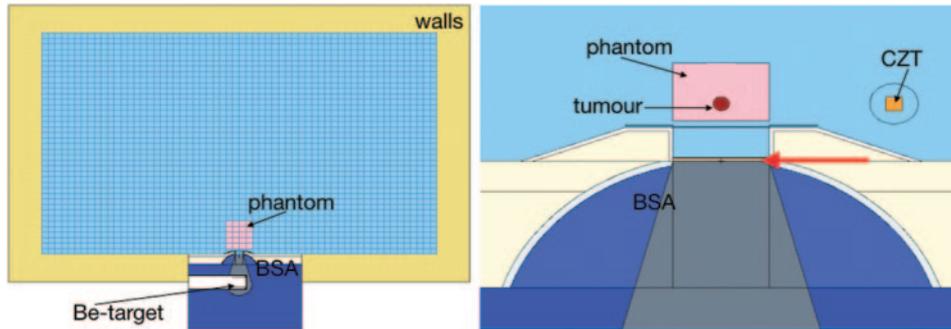
Fig. 1. – MCNP6 simulated geometries: to study the $(n + \gamma)$ background in the treatment room (left); to evaluate the relevant physical quantities inside the CZT detector (right). In both panels, pink represents the phantoms; in the right panel it is possible to see the shallow tumour (red circle) and the $20 \times 20 \times 20 \, \text{mm}^3$ CZT detector (orange square). The surface from which neutrons are generated by the simplified source is labeled by the red arrow.

the wide band gap $(1.57 \, \text{eV})$ [10]. Finally, the possibility to easily realise pixels/strips electrodes by standard photolithography allows to obtain high-spatial-resolution imaging detectors. In addition, CZT technology is receiving significant attention from the scientific community, including the field of more general nuclear medicine, as reported by the commercial small FOV SPECT machines for Myocardial Perfusion Imaging (MPI) [11] and the first prototypes for Breast Molecular Imaging (BMI) applications [12].

A preliminary characterisation of a small $5 \times 5 \times 20 \, \text{mm}^3$ CZT detector in terms of detection efficiency and energy resolution in the energy range peaked around $500 \, \text{keV}$ has been recently performed by our team [13] proving, in ideal and reference conditions, encouraging performances for future BNCT-SPECT application.

2˙1. *Monte Carlo simulated set-up and calculations*. – The present work is entirely based on Monte Carlo simulations performed using the MCNP6 Monte Carlo code [14]. The set-up of the calculations to study the $(n + \gamma)$ radiation background is shown in the left panel of fig. 1. The entire treatment room of an Accelerator-Based BNCT facility (AB-BNCT) is simulated. In blue, grey and white, at the bottom side of the view, there is the Beam Shaping Assembly (BSA) facing the Be-target used to produce neutrons from the $^9\text{Be}(\text{p,n})^{10}\text{B}$ threshold reaction [15]. The neutron beam employed in these simulations is peaked in the epithermal region (around ≈ 1–$10 \, \text{keV}$) and has a total neutron flux at the beam port higher than $10^9 \, \text{cm}^{-2}\text{s}^{-1}$. The port from which the neutron beam comes out is centred in the bottom side wall of the shown transversal section.

To study the background inside the room we used a periodic grid (MCNP6 mesh tally) made of $10 \, \text{cm}^3$ cubes which completely fills the air volume and asked for the code to calculate the mean values of neutron and photon fluxes in each cube of the grid. To better simulate the CZT working conditions expected in the BNCT-SPECT, a polyethylene phantom of $40 \, \text{cm} \times 50 \, \text{cm} \times 50 \, \text{cm}$ was placed in front of the beam port.

On the other side, the right panel of fig. 1 is a zoom at the beam port region to show the simplified patient irradiation set-up used to calculate the responses of a $20 \times 20 \times 20 \, \text{mm}^3$ monolithic CZT detector. The detector is positioned at $14 \, \text{cm}$ from the lateral surface of an $8.5 \times 12 \times 12 \, \text{cm}^3$ tissue equivalent phantom [16], which, in turn, is at $3 \, \text{cm}$ from the beam port and simulates a human head. A $1 \, \text{cm}$ radius ICRU-44 tissue sphere was placed inside the phantom to represent a shallow tumour.

TABLE I. – *Neutron and photon fluxes in the reference position from the beam port axes.*

E (MeV)	Neutron ϕ (cm^{-2}s^{-1})	E (MeV)	Photon ϕ (cm^{-2}s^{-1})
$4 \cdot 10^{-7}$	$5 \cdot 10^6$	0.45–0.50	$1.3 \cdot 10^6$
$4 \cdot 10^{-7}$–$1 \cdot 10^{-6}$	$5 \cdot 10^5$	2.1–2.3	$1.7 \cdot 10^7$
$1 \cdot 10^{-6}$–4	$8.3 \cdot 10^6$	0.0–2.3	$1.3 \cdot 10^8$

Due to the big dimensions of the treatment room ($4\,\mathrm{m} \times 6\,\mathrm{m} \times 3.5\,\mathrm{m}$) compared to the extremely small ones of the CZT detector ($8 \cdot 10^3\,\mathrm{mm}^3$) and with the goal of keeping under control the calculation time (less than 24 hours per single simulation), all the quantities (fluxes, reaction rates, photon counts) calculated inside the CZT volume were obtained using a translated and simplified neutron-only source which was defined starting from the energy and angular distributions of the neutrons at the beam port after having been generated by the Be target and moderated by the BSA. To further speed up calculations, Monte Carlo transport was stopped once the particle (neutron, photon or electron) enters one of the treatment room walls (yellow ochre in the left panel of fig. 1). The reaction rates (and thus the photon/s emission) due to 50 ppm of ^{10}B inside the shallow tumour, the ^{1}H captures in the sphere and the ^{113}Cd captures in CZT were estimated using this simplified source and then were used to generate the photon emissions recorded in the simulated spectra. Thus, the obtained spectra do not include the contribution coming from, for example, the photon background of the treatment room. This refinement of the simulated spectra is presently underway.

Considering the natural cadmium present in the CZT molecular structure, we expect a significant interaction between thermal neutrons and the ^{113}Cd isotope ($\approx 13.5\%$ of isotopic abundance) through the radiative capture reaction ^{113}Cd(n,γ)^{114}Cd [17]. The two most probable γ emissions are at energies of 558 keV ($\%I_\gamma \approx 75\%$) and 651 keV ($\%I_\gamma \approx 14\%$), pretty close to the BNCT signal. Thus, a careful estimation of the ^{113}Cd reaction rate must be performed to understand how much these parasitic photons degrade the CZT spectrum around 478 keV. Due to the high value of the capture cross-section on ^{113}Cd at thermal energies ($\approx 2 \cdot 10^4$ barn at 0.5 eV cutoff), we expect a significant attenuation of the incident neutron flux by even few millimeters of natural cadmium. For this reason, we calculated the neutron fluxes and the reaction rates in concentrical sub-volumes of the monolithic CZT crystal, as illustrated in the left panel of fig. 3.

3. – Results

3˙1. *Radiation background in the treatment room.* – Figure 2 shows neutron and photon flux distributions in the treatment room, respectively left and right panel. Table I reports in more detail the fluxes at different energy bins in a reference position (≈ 25–$30\,\mathrm{cm}$ from the beam port axes). All these values have been obtained assuming that the accelerator was working at its maximum power.

3˙2. *Neutron interactions in CZT material.* – Table II shows the reaction rates induced on the ^{113}Cd isotope and due to total energy neutron spectrum. These values should be compared to the corresponding results obtained on ^{10}B and ^{1}H isotopes inside the spherical tumour volume, respectively equal to $5.3 \cdot 10^7$ and $5.4 \cdot 10^8$ reaction/s over
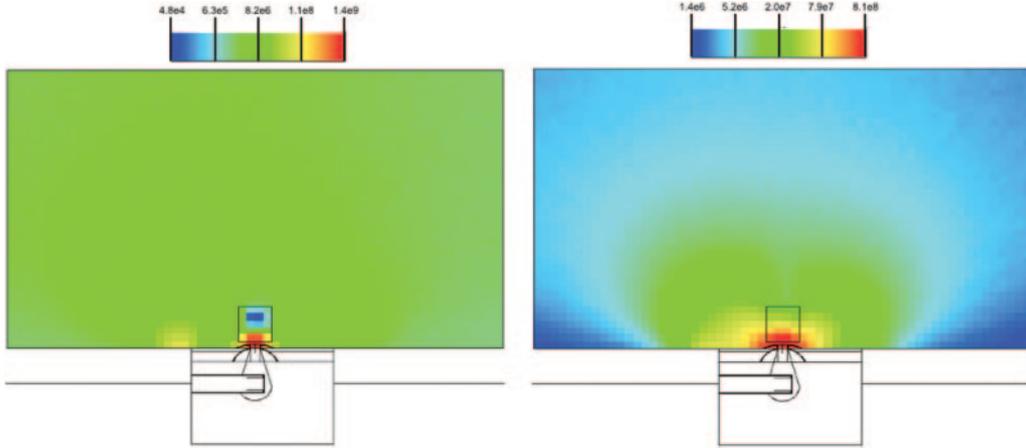
Fig. 2. – Transversal maps of neutron (left) and photon (right) fluxes $(\text{cm}^{-2}\text{s}^{-1})$ in the patient BNCT treatment room. The cuts are taken at the middle point of the beam port vertical axes to show the maximum values of the fluxes. The white geometry visible in the bottom part of the pictures is the (BSA + Be-target) source system.

TABLE II. – *Neutron capture reaction rates induced by the whole neutron spectrum in the sub-volumes of the CZT crystal. Numbers are obtained assuming the neutron source was working in such a way that $1 \cdot 10^9 \, n/cm^2 s$ intercepted the entrance face of the tissue equivalent phantom.*

CZT sub-volume (see fig. 3)	Reaction rate (s^{-1})
volume I	$2.45 \cdot 10^7$
volume II	$1.30 \cdot 10^6$
volume III	$5.67 \cdot 10^5$
volume IV	$5.97 \cdot 10^5$
volume V	$2.97 \cdot 10^5$

the whole solid angle. Taking into account the geometrical acceptance under which the photon emissions from the tumour sphere reach the CZT detector $(\approx 7.6 \cdot 10^{-4})$, the attenuation and scatter due to the phantom and the intrinsic detection efficiency at $478 \, \text{keV}$ and $2.2 \, \text{MeV}$, the expected counting rates under the photopeaks are respectively $3.1 \cdot 10^3$ and $2.5 \cdot 10^4$ cps. Figure 3 illustrates the variation of the neutron spectrum profile with increasing crossed thickness of CZT. It helps to understand the inhomogeneous induction of capture reactions in the detector by thermal neutrons.

3'3. *Preliminary evaluation of the photon spectrum recorded by the CZT detector*. – The left panel of fig. 4 shows the simulated spectrum obtained with the emission probabilities calculated in the previous section. We can see that the two ^{113}Cd peaks are clearly visible and induce a Compton edge which severely disturbs the detection of the $478 \, \text{keV}$ γ-ray from ^{10}B reactions. Indeed, from table II and neglecting in the first approximation the corrections due to the detection efficiency on ^{113}Cd γ-rays, we could roughly expect a factor 10^4 in favour of ^{113}Cd signals. As a consequence, we performed
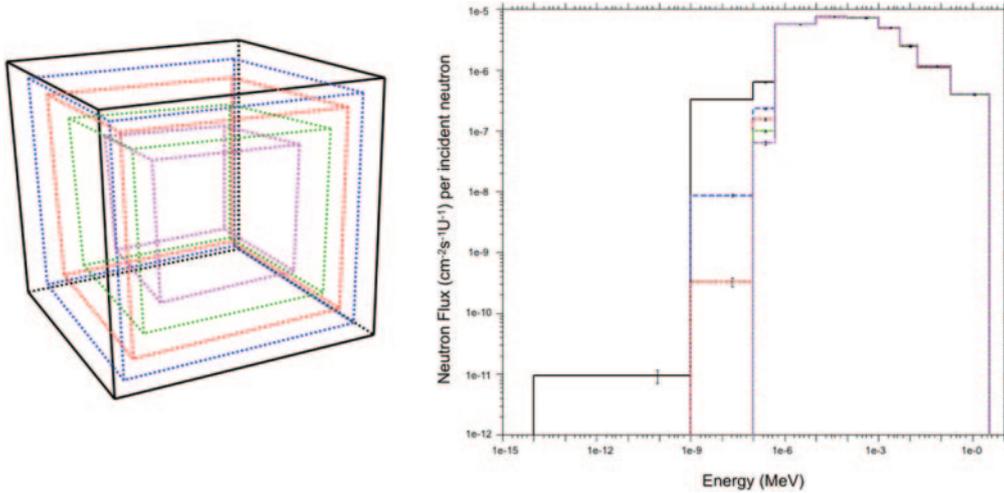
Fig. 3. – Left: scheme of the cubic sub-volumes into which the CZT monolithic volume was divided (not in scale). All the cubes have the same centre. Right: neutron flux spectra after having crossed different thicknesses of the CZT detector. Legend: black: 20 mm side cube (volume I); blue: 18 mm side cube (volume II); red: 16 mm side cube (volume III); green: 14 mm side cube (volume IV); pink: 10 mm side cube (volume V).

a second simulation in which the emission probabilities for ^{113}Cd γ-rays were biased by a factor 10^{-4}. The right panel of fig. 4 shows the result of this ideal situation where the 478 keV signal is clearly detected and resolved from the ^{113}Cd γ-rays.

Finally, we performed simulations in which the photon emission probabilities were taken at their real expected values and surrounding the CZT volume by ^{6}Li-enriched LiF layers of 2, 3 or 5 mm thickness to exploit ^{6}Li as a shielding element against thermal neutrons (left panel of fig. 5).

4. – Discussion

Figure 2 and table I show that at $\approx$ 25–30 cm from the beam axes (a reasonably suitable position for a CZT detectors ring) the (n + γ) background is significant, thus it will be necessary to develop proper shields against neutrons as well as photons to reduce the noise signal induced in the CZT detector.

Table II shows the reduction in the intensity of neutron capture reactions as a function of increasing depth inside the CZT detector. We can see that most of the reactions take place on the surface of the detector, producing a huge number of γ-rays heavily affecting the final recorded spectrum (see fig. 4, left panel). As a countermeasure, we simulated increasing thicknesses of ^{6}Li-enriched LiF layers which avoid the interaction of thermal neutrons with the CZT material. As shown in the left panel of fig. 5, after 2 mm ^{6}Li-enriched LiF layer the thermal neutron absorption has already reached a sort of saturation condition, but it is enough to restore a clear 478 keV signal in the simulated spectrum. The gain coming from a further increase in LiF thickness is not significant and due to the quite high cost of the enriched compound such strategy is not justified. We are now left to face a non-trivial problem to further improve the BNCT spectrum recorded by the CZT detector. Two mm of ^{6}Li-enriched LiF remove very well the thermal component
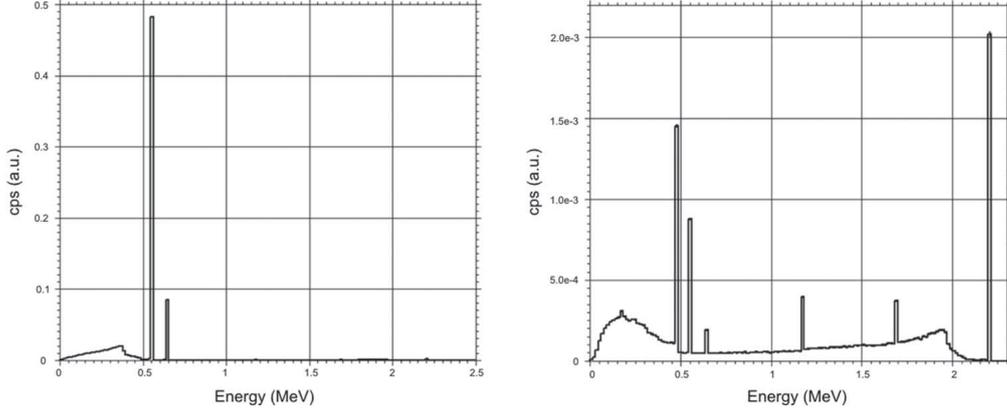
Fig. 4. – Left: photon spectrum recorded by a $20 \times 20 \times 20 \, \text{mm}^3$ CZT detector facing a 50 ppm ^{10}B-enriched shallow tumour. Real emission probabilities for the ^{113}Cd capture γ-rays. Right: photon spectrum recorded in the same condition as the first one, having reduced by a factor 10^{-4} the emission probabilities for the main γ-rays from ^{113}Cd capture.

of the neutron field. Anyway, this leads to a hardening of the neutron spectrum (see right panel of fig. 5). At the "over-thermal" energies left by ^{6}Li the neutron capture cross-section of ^{113}Cd shows several resonances between 10 eV and 10 keV (exactly the energy range in which our primary neutron beam is peaked), with values ranging from approximately 1 barn up to 10^3 barns. This residual high-energy neutron spectrum carries on the activation of cadmium and is the objective towards which to address any further attempt for further reducing the CZT spectra background.
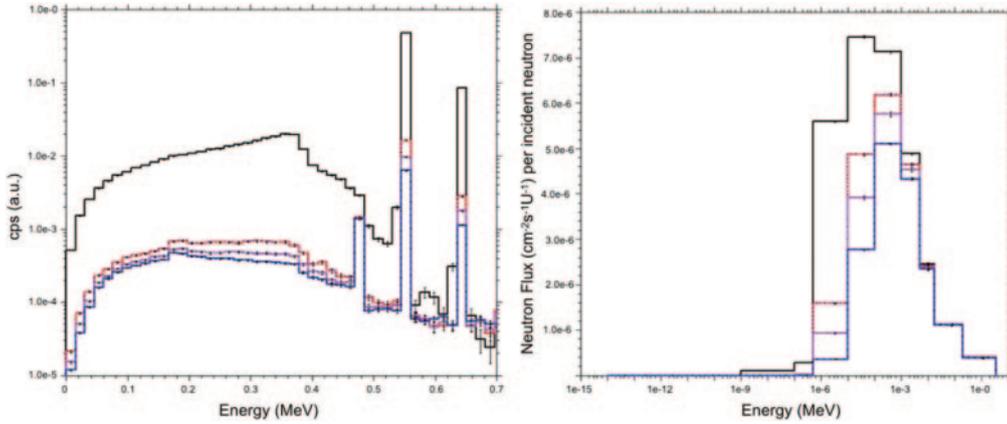

Fig. 5. – Left: photon spectra recorded by a $20 \times 20 \times 20 \, \text{mm}^3$ CZT detector facing a 50 ppm ^{10}B-enriched shallow tumour and surrounded by 0 (black line), 2 (red line), 3 (pink line) or 5 mm (blue line) ^{6}Li-enriched LiF layers to reduce the thermal neutron capture reactions induced on the ^{113}Cd isotope. Right: neutron flux spectra per incident neutron inside the CZT detector surrounded by 0 (black line), 2 (red line), 3 (pink line) or 5 mm (blue line) ^{6}Li-enriched LiF layers.

5. – Conclusion

In this work we evaluated the (n + γ) background in the treatment room of an accelerator-based BNCT clinical facility to support the INFN 3*CaTS* project developing CZT detectors to be employed as the base sensitive elements of a BNCT-SPECT. Furthermore, we studied the contribution to the photon spectrum due to the ^{113}Cd(n,γ)^{114}Cd capture reaction. These preliminary numbers helped us in understanding the minimal shielding requirements to get a reasonable measurement of the 478 keV γ-ray of interest in BNCT therapeutic dose monitoring. Finally we simulated the photon spectrum recorded by the CZT detector when facing a shallow tumour enriched by 50 ppm of ^{10}B.

This is a first, preliminary study of the mixed radiation field we expect in a next generation, accelerator-based BNCT facility. The complexity of the situation in which we have to perform a very precise measurement of a significantly low signal is pointed out by the different aspects we focused on in this simulation-based study. Further calculations are presently on-going to get closer to a real expected spectrum recorded by a CZT detector.

REFERENCES

[1] Moss R. L., *Appl. Radiat. Isot.*, **88** (2014) 2.
[2] Savolainen S. *et al.*, *Phys. Med.*, **29** (2013) 233.
[3] Imahori Y. *et al.*, *J. Nucl. Med.*, **39** (1998) 325.
[4] Kobayashi T. *et al.*, *Med. Phys.*, **27** (2000) 2124.
[5] Manabe M. *et al.*, *Rep. Pract. Oncol. Radiother.*, **21** (2016) 102.
[6] Manabe M. *et al.*, *Appl. Radiat. Isot.*, **118** (2016) 389.
[7] Minsky D. M. *et al.*, *Appl. Radiat. Isot.*, **67** (2009) S179.
[8] Minsky D. M. *et al.*, *Appl. Radiat. Isot.*, **69** (2011) 1858.
[9] Winkler A. *et al.*, *Appl. Radiat. Isot.*, **106** (2015) 139.
[10] Del Sordo S. *et al.*, *Sensors*, **9** (2009) 3491.
[11] Miyagawa M. *et al.*, *Ann. Nucl. Cardiol.*, **1** (2015) 18.
[12] Hruska C. B., *Am. J. Roentgenol.*, **208** (2017) 275.
[13] Fatemi S. *et al.*, *Nucl. Instrum. Methods A*, **903** (2018) 134.
[14] Goorley T. *et al.*, *Nucl. Tech.*, **180** (2012) 298.
[15] Kreiner A. J. *et al.*, *Rep. Pract. Oncol. Radiother.*, **21** (2016) 95.
[16] White D. R. *et al.*, ICRU Report, **44** (1989) 1.
[17] McGregor D. S. *et al.*, *Nucl. Instrum. Methods A*, **381** (1996) 498.